

Metal–silicate partitioning of Mo and W at high pressures and temperatures: Evidence for late accretion of sulphur to the Earth

Jon Wade^{*}, Bernard J. Wood, James Tuff

Department of Earth Sciences, University of Oxford, South Parks Road, OXFORD OX1 3AN, UK

Received 2 December 2010; accepted in revised form 17 January 2012; available online 28 January 2012

Abstract

In order to place better constraints on the conditions of core formation on Earth and other planetary bodies we have performed experiments to determine the partitioning of Mo and W between liquid Fe-rich metal and liquid silicate at pressures of 1.5–24 GPa and temperatures of 1803–2723 K. Experiments performed in MgO capsules at 1.5 GPa/1923 K indicate that Mo is in the +4 oxidation state in the silicate at oxygen fugacities $>2\log$ units below the IW (Fe–FeO) buffer. In contrast W^{6+} is the dominant tungsten oxidation state in the silicate at 1.5 GPa/1923 K and 1.8–3.3 log units below the IW buffer. When our 15 data for pressures between 6 and 24 GPa are combined with those of [Cottrell et al. \(2009\)](#) we find evidence neither for a change in oxidation state of W above 6 GPa nor for a change in pressure dependence of partitioning in the experimental fO_2 range.

Metal–silicate partitioning of both Mo and W shows strong dependence on silicate melt composition with both elements becoming more siderophile as the melt becomes more SiO_2 -rich. Although the trends in the partitioning data can be related to silicate melt composition in terms of the ratio of nonbridging oxygens to tetrahedral cations ($\frac{NBO}{T}$) we find that use of a regular solution model for the silicate melt results in a significantly better fit to the data.

We combined our results with those in the literature to obtain partitioning equations applicable to the Earth. In terms of weight partitioning we define D_i^{wt} and $(K_D^i)_{wt}$ as follows:

$$(D_{Mo}^{wt}) = \frac{[Mo]_{met}}{[Mo]_{sil}}; (D_{Fe}^{wt}) = \frac{[Fe]_{met}}{[Fe]_{sil}};$$

$$(K_D^{Mo})_{wt} = \frac{(D_{Mo}^{wt})}{(D_{Fe}^{wt})^2}; (K_D^W)_{wt} = \frac{(D_W^{wt})}{(D_{Fe}^{wt})^3}$$

The experimental data, when corrected for compositional effects, yield the following expressions for a pyrolite mantle:

$$\log(K_D^{Mo})_{wt} = 1.44 - \frac{143}{T} - \frac{167P}{T} (0.19)$$

$$\log(K_D^W)_{wt} = 1.85 - \frac{6728}{T} - \frac{77P}{T} (0.24)$$

The value in brackets corresponds to 1 standard error of the fit. These expressions were combined with the continuous accretion model of [Wade and Wood \(2005\)](#) to investigate the constraints which they place on the accretionary process. We find, however, that, for accretionary paths consistent with the silicate Earth contents of Ni, Co, V, Cr and Nb, W should partition twice as strongly into the core as Mo. This is in stark contrast to the estimated core–mantle partition coefficients of ~ 40 for W and 90–140 for Mo. Neither changes to the accretionary path nor the assumption of partial disequilibrium can readily alter this result. The answer appears to reside with the identity of one of the light elements in the core.

^{*} Corresponding author.

E-mail addresses: Jon.wade@earth.ox.ac.uk (J. Wade), Bernie.Wood@earth.ox.ac.uk (B.J. Wood), James.Tuff@earth.ox.ac.uk (J. Tuff).

We investigated the effect of S on our accretionary model by adding 2% of this element (consistent with cosmochemical estimates) to the core. If S is added at constant S/Fe ratio throughout accretion the net effect is negligible. If, however, S is added exclusively during the last 10–20% of accretion D_{Mo} and D_{W} become consistent with the silicate Earth contents of these elements. Only small additional adjustments to the model are required to accommodate changes in partitioning of Ni, Co, V, Cr and Nb. We conclude that the Mo and W contents of the silicate Earth indicate that S (and other moderately volatile elements) was added to the Earth during core formation but only during the last $\sim 20\%$ of accretion. This conclusion is the same as that reached by Schönbachler et al. (2010) from the Ag isotopic composition of silicate Earth.

© 2012 Elsevier Ltd. All rights reserved.

1. INTRODUCTION

Information on the conditions of core formation on Earth and other planetary and asteroidal bodies depends primarily on an understanding of how siderophile elements such as Ni, Co, Mo and W partition themselves between cores and mantles during metal segregation. The observation that the silicate Earth has approximately the same ratios of refractory lithophile elements as chondritic meteorites (Allègre et al., 1995; McDonough and Sun, 1995) implies that all refractory elements are present in the bulk Earth (core plus mantle) in approximately chondritic proportions. This enables estimation of the core–mantle partition coefficients for siderophile elements D_{M} defined as follows:

$$D_{\text{M}} = \frac{[\text{M}]_{\text{metal}}}{[\text{M}]_{\text{silicate}}} \quad (1)$$

where $[\text{M}]$ is the concentration of element M in the phase of interest. These partition coefficients depend on pressure, temperature and oxygen fugacity, in the latter case because transfer from silicate to metal involves a change of oxidation state:



Applying the current concentration of FeO in Earth's mantle of about 8 weight% and of Fe in the core of 80% (Allègre et al., 1995; McDonough and Sun, 1995), reaction (2) yields an apparent $f\text{O}_2$ of core segregation approximately $2 \log f\text{O}_2$ units below Fe–FeO (iron–wüstite, IW) equilibrium. Given experimental data on metal–silicate partitioning as a function of pressure, temperature and oxygen fugacity, this leads to constraints on the conditions under which the core segregated from silicate Earth. A first order observation is that pressures appear to have been high (~ 40 GPa) during the later stages of the process (Thibault and Walter, 1995; Li and Agee, 1996; Righter, 2003; Wade and Wood, 2005). This led to the ‘deep magma ocean’ hypothesis which, at its simplest, is considered to refer to core–mantle equilibration at a single pressure, temperature and mantle composition. In this interpretation (Li and Agee, 1996; Righter and Drake, 1997) droplets of metallic liquid descended through a 700 km deep magma ocean, equilibrating with the silicate liquid as they fell (Rubie et al., 2003). After ponding at the base of the magma ocean the metallic iron descended in large diapirs through the

more viscous lower mantle without further equilibration hence recording partitioning at the pressures and temperatures at the base of the magma ocean.

Further refinement of the metal–silicate equilibration model, such as consideration of changing pressure–temperature–oxygen fugacity conditions as the planet grew (Wade and Wood, 2005) or of partial disequilibrium between metal and silicate (Rudge et al., 2010) depends on improving the metal–silicate partitioning database. In this context there have been numerous studies of Ni and Co partitioning and a recent comprehensive programme of experiments (Kegler et al., 2008). Although W has also been addressed in detail recently (Cottrell et al., 2009) there are relatively few data on the important siderophile element Mo. The principal aim of this study was, therefore to determine Mo partitioning as a function of pressure, temperature and oxygen fugacity at conditions up to 24 GPa and 3000 K. Because of the geochemical similarities between Mo and W, we also added W to a number of our experiments in order to determine any profound differences between Mo and W behaviour at high pressures and temperatures.

2. EXPERIMENTAL AND ANALYTICAL PROCEDURES

Experimental pressure and temperature conditions and compositions of the starting materials are shown in Table 1. All starting materials were based on a mix of $\sim 50\%$ Fe metal (doped in some cases with S and/or Si as FeS and FeSi₂) and $\sim 50\%$ silicate. In most cases the latter approximated the 1.5 GPa eutectic composition in the system anorthite–diopside–forsterite (An₅₀Di₂₈For₂₂) (Presnall et al., 1978). Mo, W and (in some cases) Ni, Co and other trace elements were added to the metal–silicate mixtures as analytical grade oxides. The starting materials were ground under acetone to ensure fine grain size and homogeneity, before being dried prior to the experiment.

Experiments were performed at 1.5, 6 and 24 GPa, using an end-loaded Boyd–England-type piston–cylinder apparatus, a Walker-type multi-anvil apparatus (Walker et al., 1990) and a split-sphere multi-anvil apparatus respectively. Most 1.5 GPa experiments used a $\frac{1}{2}$ -inch BaCO₃–SiO₂ glass assembly with a graphite heater (e.g. McDade et al., 2002). Both the internal spacers and the capsule material consisted of polycrystalline machineable MgO that had been fired at 1000 °C to ensure dryness. Additional experiments were performed in silica glass capsules and in

Table 1
Starting comp and experimental run conditions.

Experiment	Pressure GPa	Temp K	Capsule material	Run duration mins	Starting compositions - Silicate		Metal Fe+	NBO/T	log f_{O_2} (rel to IW)
						FeO added?*			
1009	1.5	1923	MgO	75	Anorthite (An)	3%	-	2.5	-3.09
1011	1.5	1923	SiO ₂	60		7%	-	0.6	-2.42
1012	1.5	1923	MgO	25		7%	-	2.8	-2.72
1014	1.5	1923	MgO	50		-	-	2.1	-3.09
1019	1.5	1923	SiO ₂	40		10%	-	0.6	-2.19
1020	1.5	1923	SiO ₂	45		5%	-	0.6	-2.41
1021	1.5	1923	MgO	50		5%	-	2.6	-2.45
1022	1.5	1923	MgO	50		5%	~2.5% S*	2.3	-2.37
1023	1.5	1923	MgO	65		5%	~7% S* + CoO	2.6	-2.22
1024	1.5	1923	MgO	80		5%	~12% S* + CoO	2.6	-2.15
1025	1.5	1923	MgO	20		10%	-	2.5	-2.08
1026	1.5	1923	MgO	140		-	7% S*	2.6	-2.54
1027	1.5	1923	MgO	115	Diopside (Di)	-	12% S*	2.6	-2.17
1028	1.5	1923	MgO	38		-	7% S*	2.4	-2.39
1029	1.5	2173	MgO	5	Forsterite (Fo)	-	-	2.8	-2.65
1030	1.5	1748	C	77		-	-	1.2	-1.87
1031	1.5	1923	C	6		-	-	1.2	-1.77
1032	1.5	1923	MgO	45		-	50% FeS	2.7	-2.43
720	1.5	1803	C	22	45% Di, 36% An, 19% Fo	25%	-	2.3	-0.67
721	1.5	1803	C	16	40% Di, 30% An, 18% Q, 12% Fo	40%	-	1.7	-0.40
745	1.5	1983	MgO	35	75% Di, 25% Q	20%	-	4.0	-1.77
755	24	2473	MgO	2	Pyrolite	5%	-	2.6	-2.14
758	24	2673	MgO	2		-	-	2.4	-2.28
922	1.5	1923	MgO	40	28% Di 50% An 22% Fo	10%	20% FeS	2.6	-2.24
923	1.5	1923	MgO	35		10%	40% FeS	3.0	-2.36
926	1.5	1923	MgO	42		19%	-	2.8	-1.83
929	1.5	1923	MgO	50		10%	15% FeS	2.6	-2.67
942	1.5	2273	C	10	21% Di, 37% An, 17% Fo, 25% MgO	15%	-	3.1	-1.10
BJW1010	1.5	2723	C	2		-	4%Ni+4%MoO ₃ +4%WO ₃	4.0	-2.75
BJW1013	1.5	2553	MgO	4		-	4%Ni+4%MoO ₃ +4%WO ₃	3.9	-2.45
BJW1014	1.5	2593	MgO	4		-	4%Ni+4%MoO ₃ +4%WO ₃	4.0	-2.91
BJW1016	1.5	1923	MgO	45		8%	7%Mo	0.7	-2.22
C10	6	2123	MgO	5	Anorthite (An)	10%	FeS	3.0	-1.96
C15	6	2123	MgO	5		10%	FeS	2.9	-2.22
C18	6	2123	MgO	5		-	Ni + CoO	2.6	-2.80
C19	6	2123	MgO	5		15%	Ni + CoO	2.8	-2.06
C20	6	2123	MgO	5	Diopside (Di)	20%	Ni + CoO	3.0	-1.85
C21	6	2123	MgO	5		35%	Ni + CoO	3.1	-1.53
C25	6	2123	MgO	5	Forsterite (Fo)	5%	MoO ₃ +WO ₃ + FeSi ₂	2.9	-3.41
C26	6	2123	MgO	5		10%	MoO ₃ +WO ₃ + FeSi ₂	2.3	-2.99
C28	6	2123	MgO	5		15%	MoO ₃ +WO ₃ + FeSi ₂	3.1	-2.30
C29	6	2123	MgO	5		25%	MoO ₃ +WO ₃ + FeSi ₂	3.7	-2.12
C50	6	2123	MgO	5		-	-	2.9	-2.81
C8	6	2123	MgO	5		10%	Fe 94% Ni 6%	2.8	-2.42
JT1002	1.5	1923	MgO	60		10%	Fe 94% Ni 6%	2.6	-2.64
JT1003	1.5	1923	MgO	60		10%	Fe 94% Ni 6%	2.7	-1.91
JT1004	1.5	1923	MgO	60		10%	Fe 94% Ni 6%	3.0	-2.05
JT1005	1.5	1923	MgO	60		10%	Fe 94% Ni 6%	2.2	-2.24
JT1006	1.5	1923	MgO	60		10%	Fe 94% Ni 6%	2.2	-2.20
1016	1.5	1923	MgO	60		10%	-	2.4	-2.22
742	16	2273	MgO	10		-	-	3.0	-2.30

* S added as FeS.

+ FeO added as percentage of silicate component.

graphite capsules (Table 1). The reasons for using different capsule materials is that each type of capsule influences the result in different ways and it is important to remove or account for these effects. In graphite capsules the metal becomes carbon saturated and carbon in the metal profoundly affects the thermodynamic properties of Mo and W dissolved in the metal (J.S.P.S., 1988). Experiments in MgO capsules lead to SiO₂-poor silicate liquids with a high ratio of non-bridging oxygens to tetrahedral cations. Silicate melt composition is known to have large effects on metal–silicate partitioning of Mo (Richter et al., 2010) and W (Cottrell et al., 2009). We therefore also performed experiments in silica glass capsules to generate melts with high SiO₂ contents and low values of non-bridging oxygens to tetrahedral cations. A combination of these experimental approaches enables compositional effects to be accounted for, as discussed below. Pressures were calibrated using the 1.6 GPa reaction: Ab = Jd + Qz at 600 °C (Holland, 1980), the 2.97 GPa quartz–coesite transition at 1000 °C (Bohlen and Boettcher, 1982) and the alumina content of

enstatite co-existing with garnet in the MgO–Al₂O₃–SiO₂ system at 3 GPa and 1600 °C (McDade et al., 2002). A friction correction of –12% was applied (McDade et al., 2002). High temperature experiments (>1900 °C) at 1.5 GPa employed similar materials with the exceptions that the outer BaCO₃ sleeve was replaced by pyrophyllite to improve thermal stability and the capsule and lid were cored from a slab of single crystal MgO (Tateho Chemical, Japan) to improve durability at high temperature. Temperature in all cases was controlled using a W₉₅Re₅–W₇₄Re₂₆ thermocouple placed either in direct contact with the capsule (single-crystal capsules) or separated from it by a 0.5 mm alumina disc (polycrystalline capsules).

Experiments at 6 GPa employed octahedra made from castable MgO-based ceramic (Ceramacast 584, Aremco Products, Inc. (Walker, 1991)) with 18 mm edges and tungsten carbide anvils with 12 mm truncations. Internal spacers and capsules were again made from MgO. The furnace assembly consisted of straight graphite heaters surrounded by outer sleeves of ZrO₂ and temperature

was controlled by a $W_{95}Re_5$ – $W_{74}Re_{26}$ thermocouple in contact with the capsule. All assembly parts, apart from the heater, were fired at 1000 °C for several hours prior to assembly. Pressure was calibrated at room temperature using transformations of Bi (I–II and III–V) and at 1200 °C using the transition of Fe_2SiO_4 in olivine to spinel (Yagi et al., 1987). Experiments at 24 GPa were performed in the multianvil laboratory of the Bayerisches Geoinstitut, Bayreuth, Germany. The pressure cell consisted of a 10 mm edge-length Cr_2O_3 -doped MgO octahedron with cylindrical ZrO_2 insulator and $LaCrO_3$ furnace. Spacers internal to the furnace were made of MgO and the single crystal MgO capsule was in direct contact with the $W_{97}Re_3$ – $W_{75}Re_{25}$ thermocouple. The octahedron was compressed using tungsten carbide anvils with 4 mm truncations.

Experiment durations were 20 min to 1 h for piston cylinder but reduced for high temperature (above 1923 K) experiments or where migration of the metal into the carbon capsule becomes significant. For multi-anvil experiments, run durations of 2 (at 24 GPa) to 5 (at 6 GPa) minutes were employed. Our previous results indicate that equilibrium is approached in 5–10 min in large internal diameter (2–3 mm) capsules and <2 min in 1.2 mm internal diameter capsules (Tuff et al., 2011). In this study we used 2–3 mm internal diameter capsules at 1923 K and 1.2 mm internal diameter capsules at higher temperatures and in cases where the capsules were made of carbon. We adjusted experiment durations (Table 1) to be consistent with our previous observations on time to approach equilibrium. Times to approach equilibrium are consistent with those of other workers (Thibault and Walter, 1995; Corgne et al., 2008; Tuff et al., 2011). All piston cylinder and multi-anvil experimental experiments were quenched after the desired duration by turning off the power to the heaters while maintaining run pressure, which was subsequently slowly released. During quenching the experiment cools through the silicate solidus in 2–3 s.

Recovered experimental products were sectioned longitudinally and mounted in acrylic before polishing. The metal invariably segregated into one or more large (>300 micron diameter) blobs surrounded by quenched liquid in the form of a mixture of glass and elongated quench crystals (Fig. 1). Fig. 1 also shows the effects of extended experimental run times in MgO capsules. Primary olivine crystals begin to grow in the silicate melt due to reaction with the capsule and may become difficult to avoid during laser-ablation analysis. The product phases were analysed using a JEOL JXA8800 electron microprobe. WDS analyses were conducted using a 20 kV accelerating voltage and 40–60 nA beam current with a 10 micron spot to improve averaging of glass and quench phase compositions. At least 25 repeat analyses were collected for the silicate and metal portions in each charge, with care being taken to avoid any possible secondary fluorescence arising from analyses that were too close to the edge of each phase (Chabot and Drake, 1999). Counting times were as follows: 30 s peak and 15 s background for major elements (e.g. Si, Al, Ca, Mg, Fe); 60 s peak and 30 s background for minor elements used as internal standards during laser ablation ICP-MS

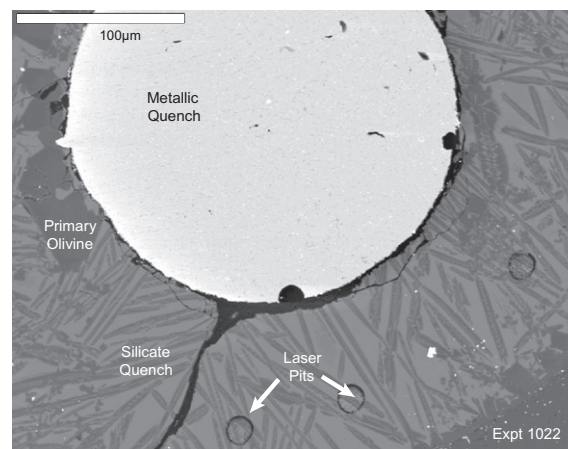


Fig. 1. Back-scattered electron image of experiment 1022 showing typical textures of products from experiments performed in MgO capsules. Note the large primary olivines and mixture of glass and quench crystals in the silicate portion of the charge. The amount of primary olivine increases with experiment duration (in this case 50 min). Note also the exsolution of some trace elements from the metal during the quench and that use of a large laser spot is needed to obtain representative average compositions.

(e.g. Ni, Co, Mo, W). A range of synthetic and natural standards was used for calibration.

Trace-element concentrations of the co-existing silicate and metal melts were determined on experimental charges by laser ablation ICP-MS using a Perkin Elmer Elan DRCII quadrupole mass-spectrometer coupled with a New Wave Research UP213 Nd:YAG laser at the University of Cambridge. Beam diameters of 60 μ m were used. The following masses were counted: ^{29}Si , ^{51}V , ^{53}Cr , ^{57}Fe , ^{59}Co , ^{60}Ni , ^{95}Mo , ^{182}W with yields calibrated on NIST 610 glass standard as the external standard. Between 4 and 10 LA-ICP-MS analyses were made of metal and silicate phases in each run product. USGS glass standard BCR-2G was used as a secondary standard to monitor the accuracy of the calibration. Internal standards for silicate and metal were the Si and Fe contents of the two phases which had been measured by electron microprobe. Metal analyses were checked by comparison of laser ICP-MS concentrations for Ni, Co, Mo and W with those obtained by electron microprobe. Agreement is generally better than $\pm 15\%$ relative using this approach (Tuff et al., 2011). Note, however, that all quoted values for Mo and W in Table 3 (metal compositions) are exclusively from microprobe analyses of the metal. Quenched silicate analyses of Mo and W (Table 2) are exclusively Laser ICP-MS results using NIST 610 glass as the external standard and BCR2G as secondary standard. Background counts were monitored for the first 20 s of each 60-s analysis and were minimised by including a 60-s ‘wash-out’ between each collection. Raw counts were collected on the ICPMS in peak-hopping mode and displayed in time-resolved format. This allowed each ablation to be monitored to identify heterogeneities such as small metal inclusions in the silicate and compositional variations with depth. All silicate analyses

Table 2
Experimental results – silicate analyses.

Experiment	Na	σ	Mg	σ	Al	σ	Si	σ	S	σ	Ca	σ	Fe	σ	Mo (ppm)	σ (ppm)	W (ppm)	σ (ppm)	Total Oxides	Total Trace Elements
1009	0.08	0.06	17.28	6.73	6.62	2.54	15.70	1.24	–	–	13.99	5.39	2.85	0.65	0.38	0.23	42.48	9.50	98.10	1.04
1011	0.03	0.00	6.46	0.03	5.76	0.06	29.18	0.07	–	–	5.12	0.05	5.62	0.16	–	–	1.34	0.62	98.44	2.37
1012	0.06	0.05	18.37	6.21	5.25	2.83	16.50	1.39	–	–	13.69	4.72	4.51	0.87	3.43	1.38	162.68	18.96	100.72	1.52
1014	0.06	0.03	16.49	5.62	7.33	1.77	16.98	0.55	0.00	0.00	13.08	4.26	2.72	0.30	0.61	0.22	35.73	2.73	99.41	1.58
1019	0.03	0.01	5.29	0.04	4.91	0.04	29.01	0.18	–	–	5.41	0.04	7.05	0.06	–	–	6.53	3.86	96.80	1.54
1020	0.03	0.01	5.89	0.10	4.83	0.17	29.89	0.11	–	–	5.55	0.08	5.46	0.08	–	–	5.16	2.20	97.71	1.41
1021	0.07	0.05	16.30	6.72	6.27	2.15	15.35	1.28	0.00	0.00	13.93	4.87	5.70	1.27	6.73	1.62	524.26	192.31	98.66	1.48
1022	0.06	0.03	15.77	6.54	6.50	1.99	16.33	0.90	0.12	0.05	12.51	4.69	6.07	0.83	3.65	0.21	381.09	18.06	98.90	1.62
1023	0.06	0.05	17.10	6.86	6.16	1.95	15.45	1.24	0.20	0.12	12.88	4.92	6.03	1.46	20.91	2.21	1681.84	98.34	99.12	1.56
1024	0.08	0.05	16.08	6.75	6.37	1.99	14.95	1.32	0.42	0.23	13.17	4.70	7.11	0.44	16.07	2.68	2004.87	180.02	98.77	1.64
1025	0.06	0.04	16.99	6.67	5.80	2.29	16.18	1.14	–	–	10.06	4.38	8.78	1.39	8.00	1.83	754.28	100.55	99.24	1.58
1026	0.08	0.04	15.91	5.14	6.46	1.72	15.48	0.90	0.32	0.13	15.71	3.93	5.15	0.83	4.45	1.13	427.01	24.28	100.75	1.02
1027	0.08	0.05	15.95	7.54	6.79	2.31	15.02	1.51	0.60	0.37	13.38	5.17	7.78	2.12	16.76	4.66	1845.92	229.09	100.86	1.24
1028	0.05	0.03	16.74	6.26	6.29	2.03	16.66	0.92	0.16	0.07	11.93	4.42	6.26	0.81	2.28	0.50	253.79	35.09	100.26	1.16
1029	0.03	0.02	23.25	2.33	6.20	1.51	15.89	0.78	0.00	0.00	7.72	2.32	4.84	0.80	6.73	0.82	254.98	36.42	101.33	1.69
1030	0.06	0.01	9.06	0.07	8.30	0.04	19.93	0.05	–	–	10.68	0.04	6.01	0.06	0.24	0.08	25.01	2.37	96.10	2.72
1031	0.05	0.01	9.26	0.05	8.33	0.07	19.66	0.15	–	–	10.60	0.07	6.46	0.08	0.58	0.08	17.53	0.92	96.37	2.48
1032	0.05	0.04	18.16	6.38	6.32	1.87	15.35	1.08	0.34	0.21	12.00	5.08	5.81	1.46	7.49	1.65	825.02	93.13	99.56	1.14
720	0.04	0.00	8.29	0.49	3.67	0.29	17.18	0.16	0.00	0.00	6.03	0.51	23.67	0.80	1.93	0.24	348.00	24.79	96.39	1.23
721	0.01	0.00	2.85	0.04	4.33	0.04	17.56	0.12	0.00	0.00	4.46	0.03	29.82	0.20	1.60	0.23	255.06	13.02	95.10	2.37
745	0.06	0.01	22.38	6.24	0.06	0.06	16.70	1.59	–	–	6.74	4.43	13.93	1.15	34.94	6.14	2685.62	657.92	100.38	2.03
755	0.14	0.00	21.95	1.63	1.35	0.37	22.04	1.29	0.00	0.00	2.38	0.57	8.84	1.90	39.30	1.44	121.26	24.56	100.97	0.99
758	0.14	0.03	21.67	0.92	2.10	0.37	22.34	1.12	0.00	0.00	2.21	0.31	7.53	1.71	26.97	14.09	45.74	24.66	100.66	1.44
922	0.08	0.04	15.39	5.64	6.21	1.84	15.45	0.96	–	–	14.47	3.89	7.33	1.14	1.78	0.83	212.01	32.39	100.97	0.39
923	0.05	0.04	19.47	6.57	4.95	2.53	15.61	1.48	–	–	10.99	5.14	6.58	1.84	4.14	0.93	420.11	142.15	100.66	0.53
926	0.07	0.04	14.22	5.19	5.69	1.56	14.53	1.13	–	–	13.15	3.59	11.87	2.12	9.93	2.05	933.57	82.21	100.09	0.60
929	0.06	0.03	17.49	5.62	6.32	1.99	15.25	1.04	0.36	0.16	13.81	4.68	4.46	0.86	1.34	0.35	156.49	31.03	98.93	0.39
942	0.03	0.01	18.22	2.35	6.04	0.63	12.02	0.39	0.00	0.00	7.96	2.18	11.46	1.22	59.87	4.66	3994.94	534.83	99.16	1.55
BJW1010	0.01	0.01	35.02	3.67	4.21	0.77	10.22	2.16	–	–	5.74	1.47	4.65	0.59	19.05	6.19	170.11	38.25	99.05	0.03
BJW1013	0.03	0.03	26.47	6.06	4.89	1.57	13.52	2.53	–	–	7.91	3.06	6.08	1.11	32.13	6.39	808.07	57.05	93.38	0.09
BJW1014	0.01	0.01	29.37	4.26	4.87	0.97	12.84	1.83	–	–	7.47	2.00	3.66	0.50	13.74	4.01	170.02	35.08	100.55	0.02
BJW1016	0.02	0.01	5.61	0.03	4.79	0.02	29.42	0.06	–	–	6.14	0.02	6.77	0.05	0.68	0.13	–	–	98.61	0.00
C10	0.01	0.02	20.66	5.28	5.57	1.31	14.88	0.77	0.14	0.26	6.97	4.18	9.88	2.22	6.92	0.76	576.09	73.98	99.24	0.66
C15	0.05	0.05	22.79	5.16	5.87	1.18	15.60	0.71	0.48	0.52	7.13	4.30	6.99	2.02	4.96	0.51	398.49	25.83	101.79	0.59
C18	0.04	0.03	21.54	4.40	6.67	1.13	15.78	0.70	0.00	0.01	9.08	4.12	3.69	0.92	–	–	13.48	1.33	99.62	0.34
C19	0.05	0.03	19.53	3.23	5.81	1.82	15.66	0.86	0.01	0.01	9.11	3.14	8.43	1.21	3.91	1.32	547.54	217.74	100.55	0.38
C20	–	–	19.80	4.17	5.64	0.98	14.73	0.64	0.00	0.01	7.76	3.37	10.90	1.75	4.29	0.66	203.79	19.91	99.93	0.44
C21	0.03	0.02	18.18	2.43	5.51	0.97	14.17	0.55	0.00	0.00	7.38	1.94	15.87	1.45	6.31	0.56	320.88	51.38	101.70	0.43
C25	–	–	23.11	6.78	4.21	2.57	17.81	1.61	–	–	9.71	7.68	2.12	1.48	2.70	0.77	11.46	1.38	100.73	0.36
C26	–	–	21.16	4.60	7.76	2.77	15.88	1.10	0.01	0.00	8.43	2.84	3.23	0.57	7.64	4.49	65.89	47.18	99.74	0.32
C28	–	–	21.42	3.89	4.58	1.27	16.07	0.71	0.00	0.00	8.54	3.48	7.34	1.22	13.41	2.27	402.73	57.08	100.00	0.46

C29	25.06	5.43	1.23	0.65	17.89	0.99	—	—	—	4.65	4.05	9.44	3.53	20.13	2.55	976.47	112.79	100.86	0.64
C50	20.34	0.79	4.86	0.84	16.48	0.54	0.01	0.02	10.68	1.22	4.03	1.53	—	—	—	30.93	0.00	98.31	0.63
C8	22.62	4.33	6.40	1.09	15.60	0.65	0.00	0.00	7.28	4.32	6.02	1.54	2.76	0.44	0.44	77.73	9.93	100.92	0.53
JT1002	19.80	7.09	6.56	2.72	15.52	1.36	0.00	0.01	11.10	5.59	4.60	1.52	1.35	0.13	0.13	43.30	3.34	99.88	0.47
JT1003	15.33	6.61	6.42	1.86	14.38	1.40	—	—	12.41	4.40	10.40	2.51	8.34	1.50	1.50	943.40	120.83	99.20	0.80
JT1004	19.92	6.56	5.36	2.42	15.13	1.95	—	—	9.39	4.16	8.67	1.14	10.18	2.87	2.87	1306.49	445.71	99.90	0.75
JT1005	14.74	4.75	6.88	1.47	16.24	0.62	0.24	0.07	13.10	3.44	6.75	0.69	2.11	0.39	0.39	296.60	51.76	99.54	0.63
JT1006	15.10	5.19	6.86	1.49	16.98	0.58	0.25	0.07	12.93	3.54	6.83	0.63	2.40	0.44	0.44	418.64	11.91	101.56	0.56
1016	15.47	7.50	6.94	2.68	14.78	1.26	0.01	0.04	12.70	5.66	7.15	2.11	13.69	2.47	2.47	1286.57	344.72	97.44	1.87
742	17.01	4.38	0.10	0.11	20.76	2.35	0.01	0.01	9.70	3.26	6.99	0.68	57.60	9.40	9.40	786.90	138.0	97.39	2.88

that exhibited evidence of metal contamination (through spikes in siderophile Mo, W and Ni concentration) were discarded. Data reduction used the GLITTER (www.es.m-q.edu.au/gemoc/glitter) software package.

3. PARTITION COEFFICIENTS – EFFECTS OF COMPOSITION, OXYGEN FUGACITY, TEMPERATURE AND PRESSURE

Major and trace element compositions of metal and silicate phases from experimental products are presented in Tables 2 and 3. In samples from experiments performed in MgO capsules, the silicate melt quenched to a mixture of glass and quench crystals (Fig 1) with, as a result of MgO dissolution from the capsule, high MgO concentrations. Experiments performed in silica glass capsules quenched to homogeneous glass containing >60% SiO₂ (Table 2). Metal–silicate partitioning of an element such as Mo involves exchange between oxidised Mo in the silicate and reduced Mo in the metal which must depend on oxygen fugacity and the oxidation state of Mo in the silicate, n :



For equilibrium (3) the equilibrium constant K_{Mo} can be defined in terms of the activities of Mo components in metal and silicate phases $a_{\text{Mo}}^{\text{met}}$ and $a_{\text{MoO}_{n/2}}^{\text{sil}}$ or their mole fractions $X_{\text{Mo}}^{\text{met}}$ and $X_{\text{MoO}_{n/2}}^{\text{sil}}$ and activity coefficients $\gamma_{\text{Mo}}^{\text{met}}$ and $\gamma_{\text{MoO}_{n/2}}^{\text{sil}}$:

$$K_{\text{Mo}} = \frac{a_{\text{Mo}}^{\text{met}} \cdot f_{\text{O}_2}^{n/4}}{a_{\text{MoO}_{n/2}}^{\text{sil}}} = \frac{X_{\text{Mo}}^{\text{met}} \gamma_{\text{Mo}}^{\text{met}} \cdot f_{\text{O}_2}^{n/4}}{X_{\text{MoO}_{n/2}}^{\text{sil}} \gamma_{\text{MoO}_{n/2}}^{\text{sil}}} \quad (4)$$

Defining the metal–silicate partition coefficient for Mo, D_{Mo} in terms of mole fractions ($\log D_{\text{Mo}} = \frac{X_{\text{Mo}}^{\text{met}}}{X_{\text{MoO}_{n/2}}^{\text{sil}}}$) and taking logarithms leads to:

$$\log K_{\text{Mo}} = \log D_{\text{Mo}} + \log \gamma_{\text{Mo}}^{\text{met}} - \log \gamma_{\text{MoO}_{n/2}}^{\text{sil}} + \frac{n}{4} \log f_{\text{O}_2} \quad (5)$$

Therefore, in order to apply experimentally measured D_{Mo} values to the Earth, it is necessary to determine the oxidation state n of Mo in the silicate together with the activity coefficients of Mo components in reduced and oxidised phases.

3.1. Activities in liquid Fe-rich metal

To calculate compositional effects in the metals, which are particularly important in the cases of C-saturated and S-bearing experiments, we used the ϵ -model (Wagner, 1962) of non-ideal interactions in Fe liquids. When modified to ensure consistency with the Gibbs–Duhem equation (Ma, 2001) this leads to the following expression for the activity coefficients of Fe and trace metal i in a multicomponent liquid alloy:

Table 3
Experimental results – metal analyses.

Experiment	Si	σ	S	σ	V	σ	Cr	σ	Fe	σ	Co	σ	Ni	σ	Mo	σ	w	σ	metals total	X _c *	Total trace elements
1009					0.02	0.005	0.04	0.005	97.66	0.46					0.25	0.02	0.26	0.01	98.23		1.93
1011	0.17	0.15	–	–	0.05	0.002	0.05	0.003	97.39	2.10	–	–	–	–	0.30	0.01	0.28	0.01	98.23		1.62
1012	–	–	–	–	0.01	0.001	0.02	0.001	98.44	0.57	–	–	–	–	0.24	0.01	0.23	0.01	98.94		1.73
1014	–	–	–	–	0.04	0.004	0.09	0.005	93.16	0.53	1.07	0.04	1.28	0.05	0.98	0.11	0.99	0.01	97.61		3.58
1019	0.11	0.01	–	–	0.05	0.001	0.05	0.002	96.63	0.34	0.59	0.00	0.68	0.03	0.48	0.03	0.46	0.01	99.06		2.17
1020	0.21	0.01	–	–	0.09	0.003	0.07	0.001	95.00	0.30	0.99	0.01	0.92	0.01	0.56	0.02	0.48	0.02	98.32		2.76
1021	–	–	–	–	0.01	0.001	0.02	0.002	93.72	0.49	1.19	0.02	1.08	0.03	0.66	0.01	0.74	0.02	97.42		3.19
1022	–	–	1.80	1.17	0.01	0.002	0.03	0.004	92.38	1.61	1.12	0.04	1.00	0.04	0.72	0.02	0.71	0.05	97.76		3.03
1023	–	–	2.08	1.47	0.01	0.002	0.01	0.001	75.72	1.76	15.89	0.72	1.28	0.05	1.04	0.13	0.61	0.08	96.77		3.27
1024	–	–	1.94	1.38	0.01	0.001	0.01	0.003	85.13	1.34	10.60	0.04	0.89	0.03	0.78	0.07	0.52	0.04	99.88		2.32
1025	–	–	–	–	0.01	0.001	0.02	0.001	94.06	0.36	1.13	0.02	1.03	0.05	0.60	0.01	0.65	0.03	97.48		2.87
1026	–	–	3.43	1.87	0.01	0.006	0.02	0.010	96.93	2.20	–	–	–	–	0.52	0.07	0.52	0.06	101.43		1.96
1027	–	–	4.53	2.74	0.01	0.001	0.02	0.003	94.12	2.92	–	–	–	–	0.87	0.11	0.69	0.08	100.25		2.20
1028	–	–	1.91	1.10	0.01	0.003	0.03	0.004	95.67	1.30	–	–	0.10	0.00	0.48	0.05	0.51	0.03	98.71		1.64
1029	–	–	–	–	0.03	0.010	0.10	0.021	92.44	1.70	0.99	0.06	1.21	0.04	0.94	0.39	0.89	0.17	96.61		3.78
1030	–	–	–	–	0.12	0.016	0.15	0.023	88.20	0.37	1.02	0.22	1.15	0.05	0.95	0.04	0.89	0.03	92.48	0.20	1.32
1031	–	–	–	–	0.23	0.032	0.20	0.034	88.53	3.12	0.74	0.19	0.97	0.07	0.77	0.11	0.73	0.07	92.17	0.21	2.80
1032	–	–	4.45	2.29	0.01	–	0.02	–	93.98	2.26	–	–	–	–	0.65	0.06	0.72	0.08	99.82		1.26
720	0.36	0.13	–	–	0.00	0.000	0.01	0.001	94.23	0.23	–	–	–	–	0.22	0.03	0.18	0.02	95.00	0.21	0.98
721	0.15	0.03	–	–	0.01	0.002	0.04	0.006	93.02	0.40	–	–	–	–	0.24	0.01	0.31	0.01	93.78	0.21	1.14
745	0.58	0.34	–	–	0.01	0.004	0.01	0.001	98.19	1.04	–	–	–	–	0.28	0.02	0.19	0.02	99.25		2.17
755	0.18	0.21	–	–	0.03	0.007	0.12	0.035	95.08	0.88	–	–	0.34	0.03	0.39	0.15	0.22	0.07	96.35		2.66
758	0.11	0.10	–	–	0.07	0.002	0.14	0.046	95.18	0.79	–	–	0.19	0.03	0.32	0.07	0.19	0.06	96.20		2.12
922	–	–	1.91	1.11	–	–	0.01	0.002	99.18	1.15	–	–	–	–	0.20	0.02	0.18	0.01	101.48		0.62
923	–	–	2.18	1.11	–	–	0.01	0.002	99.01	1.15	–	–	0.01	0.00	0.27	0.03	0.26	0.02	101.75		0.73
926	–	–	–	–	–	–	–	–	101.27	0.48	–	–	–	–	0.11	0.04	0.13	0.01	101.51		1.17
929	–	–	3.49	0.76	0.00	0.000	0.02	0.004	94.87	0.81	–	–	0.06	0.00	0.30	0.02	0.32	0.02	99.06		0.78
942	–	–	–	–	0.09	0.129	0.22	0.234	78.33	0.54	5.66	0.05	5.44	0.15	2.49	0.08	3.60	0.46	95.82	0.25	2.17
BJW1010	0.07	0.10	–	–	–	–	–	–	91.22	0.39	–	–	4.70	0.03	2.04	0.23	2.50	0.03	100.52		0.07
BJW1013	–	–	–	–	–	–	–	–	90.86	0.53	–	–	4.66	0.04	2.34	0.22	2.68	0.04	100.55		0.01
BJW1014	0.07	0.06	–	–	–	–	–	–	91.36	0.66	–	–	3.65	0.02	2.82	0.39	3.27	0.05	101.18		0.07
BJW1016	0.14	0.11	–	–	–	–	–	–	93.41	0.50	–	–	–	–	6.18	0.09	–	–	99.74		0.14
C10	–	–	2.86	1.38	0.00	0.000	0.01	0.002	87.29	5.38	–	–	2.59	0.24	0.24	0.09	0.33	0.16	93.32		2.15
C15	–	–	13.73	6.33	0.02	0.021	0.06	0.075	78.44	7.27	–	–	5.64	0.63	0.34	0.05	0.17	0.11	98.39		2.29
C18	–	–	–	–	0.02	0.006	0.06	0.007	87.85	0.95	2.33	0.02	8.47	0.09	0.22	0.03	0.26	0.01	99.21		2.51
C19	–	–	–	–	0.00	0.002	0.02	0.006	87.77	0.27	2.03	0.04	10.53	0.04	0.19	0.01	0.19	0.02	100.74		3.04
C20	–	–	–	–	0.00	0.001	0.01	0.003	86.54	0.65	1.90	0.04	9.07	0.18	0.13	0.09	0.11	0.06	97.76		1.62
C21	–	–	–	–	–	–	–	–	90.01	0.79	1.87	0.05	7.61	0.16	0.11	0.05	0.13	0.05	99.73		1.47
C25	–	–	–	–	0.06	0.007	0.11	0.010	95.71	0.62	0.03	0.00	–	–	1.62	0.13	1.19	0.06	98.72		2.33
C26	–	–	–	–	0.06	0.010	0.09	0.007	94.05	0.87	0.12	0.01	–	–	1.92	0.42	1.81	0.28	98.04		4.43
C28	–	–	–	–	0.00	0.001	0.03	0.002	93.67	0.85	0.12	0.01	–	–	1.72	0.26	1.67	0.20	97.21		2.24
C29	–	–	–	–	0.01	0.009	0.03	0.014	96.67	1.74	0.03	0.00	–	–	1.82	1.18	0.99	0.51	99.54		2.49
C50	–	–	–	–	–	–	–	–	92.89	1.39	–	–	–	–	–	–	0.24	0.01	93.13		4.69

* Mole fraction of carbon in the metallic phase, where present calculated from the Fe-C system summarised by Wood (1993) with other interactions calculated using the ϵ approach as described.

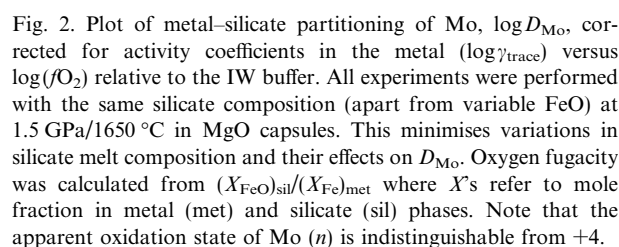


Fig. 2. Plot of metal–silicate partitioning of Mo, $\log D_{\text{Mo}}$, corrected for activity coefficients in the metal ($\log \gamma_{\text{trace}}$) versus $\log(f\text{O}_2)$ relative to the IW buffer. All experiments were performed with the same silicate composition (apart from variable FeO) at 1.5 GPa/1650 °C in MgO capsules. This minimises variations in silicate melt composition and their effects on D_{Mo} . Oxygen fugacity was calculated from $(X_{\text{FeO}})_{\text{sil}}/(X_{\text{FeO}})_{\text{met}}$ where X 's refer to mole fraction in metal (met) and silicate (sil) phases. Note that the apparent oxidation state of Mo (n) is indistinguishable from +4.

$$\begin{aligned} \ln \gamma_{\text{Fe}}^{\text{met}} = & \sum_{i=2}^N e_i' (x_i + \ln(1-x)) \\ & - \sum_{j=2}^{N-1} \sum_{k=j+1}^N e_j^k x_j x_k \left(1 + \frac{\ln(1-x_j)}{x_j} + \frac{\ln(1-x_k)}{x_k} \right) \\ & + \sum_{i=2}^N \sum_{k=2}^N e_i^k x_i x_k \left(1 + \frac{\ln(1-x_k)}{x_k} - \frac{1}{1-x_i} \right) \\ & \quad k \neq i \\ & + \frac{1}{2} \sum_{j=2}^{N-1} \sum_{k=j+1}^N e_j^k x_j^2 x_k^2 \left(\frac{1}{(1-x_j)} + \frac{1}{(1-x_k)} - 1 \right) \\ & - \sum_{i=2}^N \sum_{k=2}^N e_i^k x_i^2 x_k^2 \left(\frac{1}{(1-x_i)} + \frac{1}{(1-x_k)} + \frac{x_i}{2(1-x_i)^2} - 1 \right) \end{aligned} \quad (6)$$

$$\begin{aligned} \ln \gamma_i^{\text{met}} &= \ln \gamma_{\text{Fe}}^{\text{met}} + \ln \gamma_i^0 - \epsilon_i^j \ln(1 - x_i) \\ &\quad - \sum_{\substack{k=2 \\ k \neq i}}^N \epsilon_i^k x_k \left(1 + \frac{\ln(1 - x_k)}{x_k} + \frac{1}{1 - x_k} \right) \\ &\quad + \sum_{\substack{k=2 \\ k \neq i}}^N \epsilon_i^k x_k^2 x_i \left(\frac{1}{(1 - x_i)} + \frac{1}{(1 - x_k)} + \frac{x_i}{2(1 - x_i)^2} - 1 \right) \end{aligned} \quad (7)$$

In Eqs. (6) and (7) x_i refers to the mole fraction of i in the metal γ_i^{met} is the activity coefficient of i , γ_i^0 is the activity coefficient of i infinitely dilute in liquid Fe and ε_i^j is the

Table 4

Metal interaction parameters and infinitely dilute solute activity coefficients used in our calculations.

	V	Cr	Ni	Co	W	Mo	Si	S
γ_i^0	0.08	1.0	0.66	0.55	1	1	0.0045	(–)
$\varepsilon_{\text{Si}}^{\text{Si}}$	2.0	0.5	7.5	4.6	18.3	22	8.6	9.16
ε^{S}	–3.94	–2.1	–0.05	0.56	6.1	0.35	9.16	–5.66
ε^{M}	6.58	0	0.12	1.18	0	4.1	8.6	–5.66

 $\varepsilon_{\text{Si}}^{\text{Si}}$, ε^{S} and ε^{M} refer respectively to interaction parameters with Si, S and the element itself.All $\varepsilon_{\text{Si}}^{\text{Si}}$ values at 1873 K taken from Tuff et al. (2011) except $\varepsilon_{\text{S}}^{\text{Si}}$ which is from the Steelmaking Data Sourcebook. γ_{S}^0 not used.Metal activity calculator available at <http://www.earth.ox.ac.uk/expet/>.

interaction parameter between elements i and j . Deviations from Henry's Law are accounted for by the ε_i^j terms. The principal reason for using this approach is that many interaction parameters have been experimentally measured (J.S.P.S., 1988) and are presented in the literature in the form of ε_i^j and γ_i^0 values (Table 4). In the discussion which follows ε_i^j values have been extrapolated from 1873 K to the experimental temperature using the relationship proposed in the Steelmaking Data Sourcebook:

$$\varepsilon_i^j(T) = \frac{1873}{T} \varepsilon_i^j(1873)$$

$$\ln \gamma_i^0(T) = \frac{1873}{T} \ln \gamma_i^0(1873)$$

The interested reader may follow our activity calculations using the online calculator at <http://www.earth.ox.ac.uk/expet/>.

3.2. Oxygen fugacity effects and valence state of Mo

Experimental measurements of Mo solubility in silicate melts at 1 atm and 1400 °C (O'Neill and Eggins, 2002) indicate that $\gamma_{\text{MoO}_{n/2}}^{\text{sil}}$ is a strong function of silicate melt composition and that although Mo should be present in both 4+ and 6+ oxidation states in the oxygen fugacity range of interest to our study ($\geq 2 \log f\text{O}_2$ units below the IW buffer) the 4+ oxidation state should be dominant. This dominance becomes even more pronounced if we increase temperature at constant relative oxygen fugacity (Barin et al., 1989). In order to check the applicability of these observations to our experimental results we first had to separate the strong silicate melt compositional effects from those of oxygen fugacity. Our approach was to assume that silicate melt composition may, as a first approximation, be parameterized in terms of the ratio of non-bridging oxygens to tetrahedral cations ($\frac{\text{NBO}}{T}$). The latter compositional parameter is defined as follows (Mills, 1993):

$$\text{NBO}/T = \gamma_{\text{nb}}/\chi_t$$

where

$$\gamma_{\text{nb}} = 2[X_{\text{CaO}} + X_{\text{MgO}} + X_{\text{FeO}} + X_{\text{MnO}} + X_{\text{Na}_2\text{O}} + X_{\text{K}_2\text{O}} + 3(1 - f)X_{\text{Fe}_2\text{O}_3} - X_{\text{Al}_2\text{O}_3}]$$

and

$$\chi_t = X_{\text{SiO}_2} + 2X_{\text{Al}_2\text{O}_3} + X_{\text{TiO}_2} + 2X_{\text{P}_2\text{O}_5}$$

We considered only those experiments performed in MgO capsules under fixed pressure–temperature conditions of 1650 °C and 1.5 GPa. In order to remove silicate melt effects all experiments began with silicate consisting of Diopside₂₈Anorthite₅₀Forsterite₂₂ with varying amounts of FeO to vary oxygen fugacity. All product silicates had an extremely narrow range of ($\frac{\text{NBO}}{T}$) of 2.4–2.7 (Fig 2). By constraining the silicate compositions to this extremely narrow range we are able to investigate oxygen fugacity effects virtually independently of compositional influence. We estimate oxygen fugacity from the partitioning of Fe between metal and silicate according to the equilibrium:



From the equilibrium constant for reaction (8) it is convenient to refer oxygen fugacity to the Fe–FeO (IW) buffer as follows:

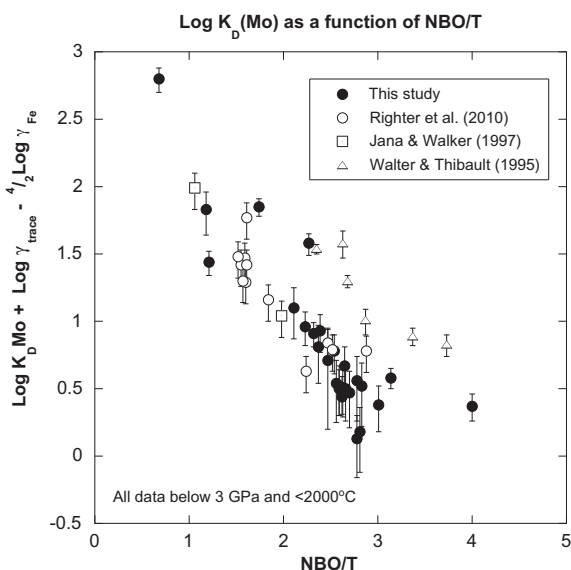


Fig. 3. Figure showing the dependence of the Mo–Fe exchange coefficient, corrected for activity coefficients in the metal

$\log K_D = \log \left[\frac{\gamma_{\text{Mo}}^{\text{met}} \gamma_{\text{Fe}}^{\text{sil}} (\gamma_{\text{FeO}}^{\text{sil}})^2}{X_{\text{MoO}_2}^{\text{sil}} (X_{\text{Fe}}^{\text{met}} / \text{Fe})^2} \right]$ on the ratio of non-bridging oxygen atoms to tetrahedral cations in the silicate melt (NBO/T).

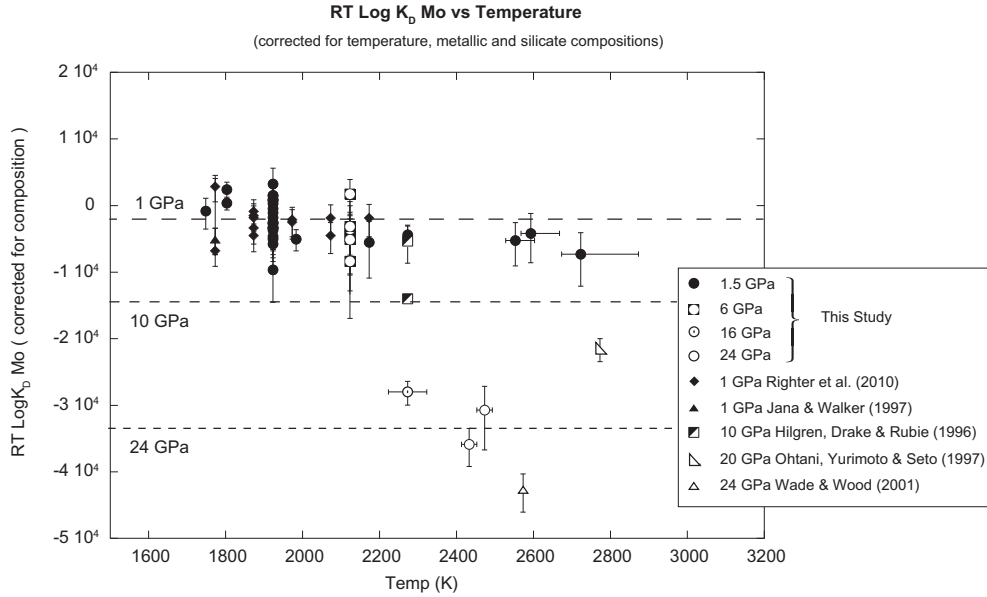


Fig. 4. Plot of $RT\log K_D(\text{Mo})$, corrected for activity coefficients in both metal and silicate phases and for temperature (Eq. (15)) versus temperature (K). As can be seen, there is a large pressure effect on $RT\log K_D(\text{Mo})$. Note that because $RT\log K_D(\text{Mo})$ is temperature-corrected the data should fall, at each pressure, on horizontal lines.

$$\log f_{\text{O}_2} = 2 \log \frac{a_{\text{FeO}}^{\text{sil}}}{a_{\text{Fe}}^{\text{met}}} = 2 \log \frac{X_{\text{FeO}}^{\text{sil}} \cdot \gamma_{\text{FeO}}^{\text{sil}}}{X_{\text{Fe}}^{\text{met}} \cdot \gamma_{\text{Fe}}^{\text{met}}} \quad (9)$$

In Eq. (9) $a_{\text{Fe}}^{\text{met}}$, $X_{\text{Fe}}^{\text{met}}$ and $\gamma_{\text{Fe}}^{\text{met}}$ refer to the activity, mole fraction and activity coefficient of Fe in the metal phase. The mole fractions of Fe and FeO in metal and oxide phases were measured by electron microprobe (Tables 2 and 3) while activity coefficients for Fe in the liquid metal were derived from Eq. (6). For simplicity we ignored the free energies and volumes of melting of Fe and FeO and initially fixed the activity coefficient of FeO in the silicate melt, $\gamma_{\text{FeO}}^{\text{sil}}$ at 1.0. In practise $\gamma_{\text{FeO}}^{\text{sil}}$ has been shown to be greater than 1.0 (O'Neill and Eggins, 2002) but, since it is a weak function of melt composition (O'Neill and Eggins, 2002) this approximation simply means that the calculated f_{O_2} is $\sim 0.3\log$ units lower than the true value but that the results are internally consistent.

Fig. 2 shows $\log D_{\text{Mo}}$ (corrected for activity coefficient in the metal) plotted as a function of oxygen fugacity for our experiments in MgO capsules at 1650 °C/1.5 GPa. As can be seen from Eq. (5), if activity coefficients of Mo components in the metal are known and those in the silicate are constant then, because of near-constant silicate composition, this plot should yield a slope of $-n/4$ where n is the oxidation state of Mo. Linear regression using the SPSS statistical package yields (one standard error in brackets):

$$\log D_{\text{Mo}} = -1.068(0.103) \log f_{\text{O}_2} + 0.452(0.250), \quad r^2 = 0.923$$

This indicates an average oxidation state of 4.27 ± 0.41 in the oxygen fugacity range between -1.9 and -3.1 log units relative to IW. Therefore, at oxygen fugacities below $-1.9\log$ units relative to IW, Mo in our experimentally-produced silicates has an oxidation state which is indistin-

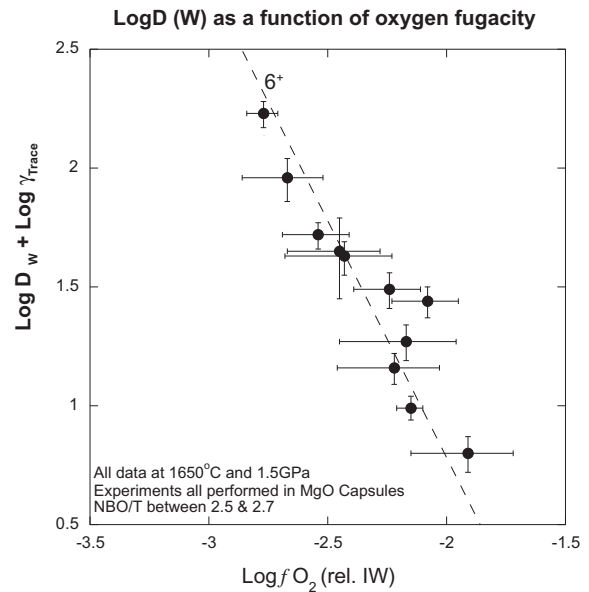


Fig. 5. Figure showing the dependence of W partition coefficient (corrected for metal activity coefficients) on oxygen fugacity for experiments performed in MgO capsules at 1.5 GPa and 1650 °C. The best fit oxidation state for W is, within uncertainty, +6. (see text).

guishable from +4. This conclusion agrees with earlier results based on the solubility of Mo in silicate melts saturated with Mo metal at known oxygen fugacity (Holzheid et al., 1994). Holzheid et al. (1994) found a change of slope in Mo solubility at 1673 K/1 bar corresponding to a change from predominantly Mo^{6+} to predominantly Mo^{4+} at 1 log unit below IW. The two sets observations,

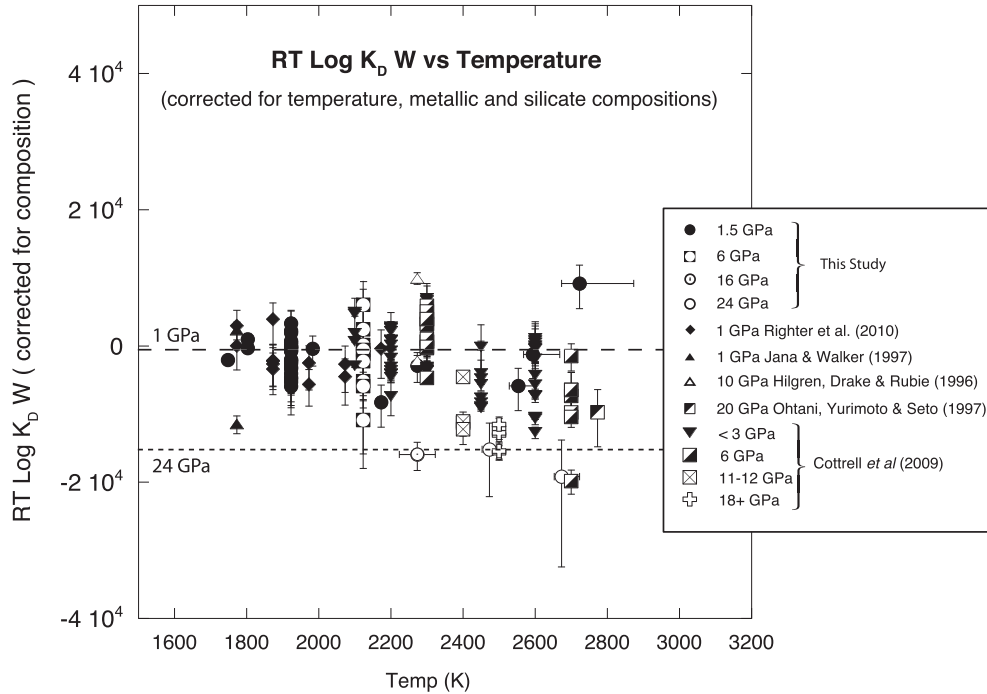


Fig. 6. Figure showing $RT\log K_D(W)$, corrected for metal and silicate activity coefficients and for temperature (Eq. (21)) plotted against temperature. Because $RT\log K_D(W)$ is temperature-corrected the data should fall, at each pressure, on horizontal lines. Note that the pressure dependence of $K_D(W)$ is much less than that of $K_D(\text{Mo})$ shown in Fig. 4.

both confirming dominance of Mo^{4+} enable us to remove oxygen fugacity from consideration as a variable at oxygen fugacities below $\sim IW-1.5$, as described below.

If we combine reactions (8) and (3), assuming that Mo dissolves in the silicate in the +4 oxidation state, then we can eliminate oxygen as a variable by turning the two reactions into one exchange reaction:



The equilibrium constant for equilibrium (10) is independent of oxygen fugacity and may be defined as follows in terms of mole fractions X_i and activity coefficients γ_i in metal and silicate phases:

$$K = \frac{X_{\text{Mo}}^{\text{met}} \gamma_{\text{Mo}}^{\text{met}} (X_{\text{FeO}}^{\text{sil}} \gamma_{\text{FeO}}^{\text{sil}})^2}{X_{\text{MoO}_2}^{\text{sil}} \gamma_{\text{MoO}_2}^{\text{sil}} (X_{\text{Fe}}^{\text{met}} \gamma_{\text{Fe}}^{\text{met}})^2}$$

Given the activity coefficients for the metal from Eqs. (6) and (7) we can define an exchange coefficient as follows:

$$K_D = \frac{X_{\text{Mo}}^{\text{met}} \gamma_{\text{Mo}}^{\text{met}} (X_{\text{FeO}}^{\text{sil}})^2}{X_{\text{MoO}_2}^{\text{sil}} \gamma_{\text{Fe}}^{\text{met}} (X_{\text{Fe}}^{\text{met}})^2}$$

Substituting K_D into the equilibrium constant and taking logarithms yields:

$$\log K = \log K_D + \log \frac{(\gamma_{\text{FeO}}^{\text{sil}})^2}{\gamma_{\text{MoO}_2}^{\text{sil}}} \quad (11)$$

At fixed pressure and temperature K is constant so the only variable which can change K_D is the ratio of activity coefficients in the silicate melt. Since $\gamma_{\text{MoO}_2}^{\text{sil}}$ has been found

to depend strongly on melt composition (O'Neill and Eggins, 2002) one would anticipate significant changes of K_D with composition.

3.3. Silicate melt effects on Mo partitioning

In order to investigate the effects of silicate melt composition on K_D we began by taking all experiments at pressures below 3 GPa and temperatures below 2000 °C and plotting $\log K_D$ versus the ratio of non-bridging oxygens to tetrahedral cations ($\frac{\text{NBO}}{T}$) (Fig. 3). As can be seen from Fig. 3 there is a strong correlation between K_D and composition with a three order of magnitude increase on going from a completely depolymerised melt ($\frac{\text{NBO}}{T} = 4$) to a completely linked tetrahedral network ($\frac{\text{NBO}}{T} = 0$). Given this correlation, however, there is scatter of up to 1 log unit in K_D at any particular value of NBO/T , presumably due to the differing effects of CaO and MgO on the activity of MoO_2 (O'Neill and Eggins, 2002). We considered this degree of scatter too great for our purposes. Therefore, in order to improve our ability to model compositional effects on Mo partitioning, we used a regular solution model in the same manner as O'Neill and Eggins (2002). For a trace component MoO_2 , dissolved in a silicate melt containing n major components the activity coefficient in a regular solution is given by:

$$RT \log \gamma_{\text{MoO}_2} = \sum_{j=1}^n \sum_{k=1}^j a_{jk} X_j X_k \quad (12)$$

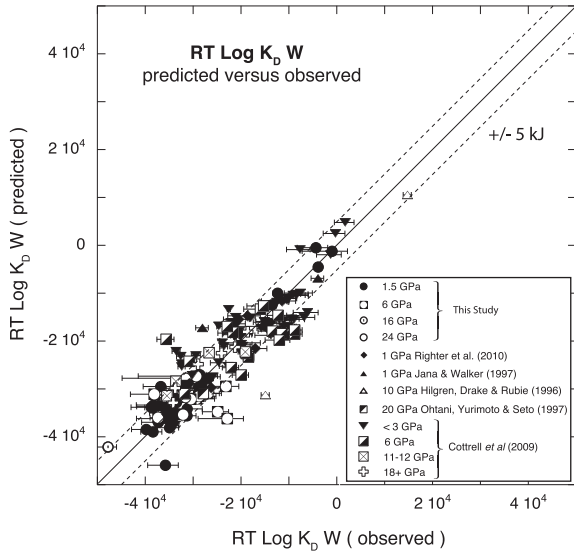


Fig. 7. Plot of calculated values of $RT \log K_D(W)$ versus observed values. Solid line is the 1:1 fit while dashed lines correspond to errors of ± 5 kJ, corresponding to 0.24–0.3 log units in K_D depending on temperature.

In Eq. (12) the a_{jk} parameters correspond to binary Margules parameters when j is equal to k and to combinations of three Margules parameters when j is not equal to k (Helffrich and Wood, 1989). Using this expression we fitted, by stepwise linear regression using the SPSS statistical package the experimental data obtained at pressures below 2 GPa and temperature less than 2000 K to the equation:

$$RT \log K_D = \text{Const} + \sum_{j=1}^n \sum_{k=1}^j a_{jk} X_j X_k \quad (13)$$

In Eq. (13) we considered terms in the major components CaO, MgO, $\text{AlO}_{1.5}$, FeO and SiO_2 and the regression accepted only those terms which passed the F -test at the 5% significance level. We obtained a fit with a standard error of the estimate (40 data points) of 2.7 kJ, corresponding to an uncertainty in K_D of ~ 0.16 log units. For comparison, when the same data are regressed versus NBO/T , we obtain a standard error of 4.2 kJ, corresponding to an uncertainty in K_D of ~ 0.25 log units. We therefore consider use of the regular solution approach justified.

3.4. Temperature and pressure effects on Mo partitioning

In our previous work (Wade and Wood, 2005) we advocated the use of end-member free energy data for the liquid oxides and liquid metals as a means of constraining the temperature effects on K_D when the experimental temperature range is small. This approach appears to work well for elements such as Ni, Co and Mn where the silicate melt effect is essentially zero and thermodynamic data are available. In the case of Mo, however, there are no data available for the melting point and entropy of melting of MoO_2 . Furthermore, the large silicate melt terms may themselves be temperature-dependent which means that the temperature term should not be too tightly constrained.

O'Neill and Eggins (2002), assumed that the properties of MoO_2 could be modelled on those of TiO_2 , leading to a temperature dependence of $RT \log K_D$ of $\sim 16 \text{ JK}^{-1}$. We used this as a guide and assumed an uncertainty of $\pm 4 \text{ JK}^{-1}$. We then fitted the experimental data (corrected for activities in the metal) to:

$$RT \log K_D = \text{Const} + \sum_{j=1}^n \sum_{k=1}^j a_{jk} X_j X_k + bT + cP \quad (14)$$

where the b parameter was varied systematically from 12 to 20 JK^{-1} to take account of the uncertainty in temperature-dependence discussed above. We included in the regression data from the literature (Walter and Thibault, 1995; Hillgren et al., 1996; Ohtani et al., 1997; Righter et al., 2010) but excluded results from experiments performed in carbon capsules in which the metal contained more than 20% Mo. This is because the Mo–C interaction parameter in the metal has only been calibrated at lower Mo contents (Suzuki et al., 1970). We found that an imposed temperature dependence of $+12 \text{ JK}^{-1}$ gave the best-fit to the data and extracted compositional and pressure terms to yield our final equation (Fig. 4):

$$RT \log K_D^{\text{Mo}} = -8040(2800) + 70820(12350) X_{\text{SiO}_2}^2 - 2.74(0.40) \times 10^5 X_{\text{CaO}} X_{\text{MgO}} + 7.3(1.6) \times 10^5 X_{\text{AlO}_{1.5}} X_{\text{CaO}} + 12T - 1390(90)P \quad \text{std error} = 3.8 \text{ kJ} \quad (15)$$

In Eq. (15) the value in brackets corresponds to 1 standard error. For mantle of MORB–pyrolite composition (Falloon and Green, 1987) Eq. (15) simplifies to:

$$\log K_D^{\text{Mo}} = 1.44 - \frac{143}{T} - \frac{167P}{T} \pm 0.19 \quad (16)$$

Note that this result refers to K_D in terms of mole fractions (Eq. (11)). On a weight basis we may define an equivalent weight K_D as follows:

$$(D_{\text{Mo}}^{\text{wt}}) = \frac{[\text{Mo}]_{\text{met}}}{[\text{Mo}]_{\text{sil}}}; (D_{\text{Fe}}^{\text{wt}}) = \frac{[\text{Fe}]_{\text{met}}}{[\text{Fe}]_{\text{sil}}}; (K_D^{\text{Mo}})_{\text{wt}} = \frac{(D_{\text{Mo}}^{\text{wt}})}{(D_{\text{Fe}}^{\text{wt}})^2} \quad (17)$$

For peridotitic compositions weight and molar K_D values are generally within 6% of one another so that Eq. (16) may also be used to calculate a weight K_D as defined in (17). This result will be applied to the conditions of terrestrial core formation in Section 4.

3.5. Tungsten–oxygen fugacity and silicate melt effects

At conditions appropriate to terrestrial core formation, previous work has found a marked dependence of tungsten partitioning on silicate melt composition and a valence state in the silicate melt varying between +6 and +4 with decreasing average oxidation state with increasing pressure (Cottrell et al., 2009). The approach taken by Cottrell et al. (2009) was similar to ours in that the $\log D_W$ dataset was broken down into subsets at fixed pressure and temperature and fixed pressure with varying temperature. They then regressed isothermal/isobaric datasets against oxygen fugacity and silicate melt composition with the latter expressed as $(\frac{\text{NBO}}{T})$. This yielded values for the valence and $(\frac{\text{NBO}}{T})$ terms which show appreciable pressure dependence. In or-

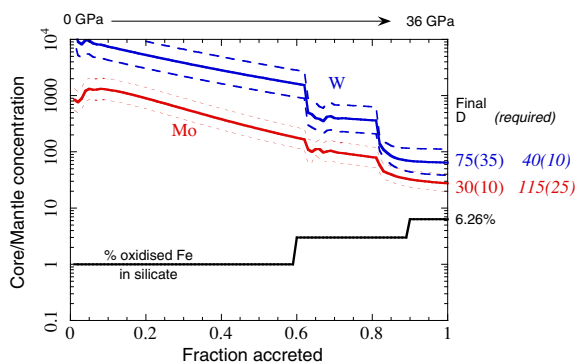


Fig. 8. Diagram showing the calculated partitioning of Mo and W between core and peridotite mantle for the continuous accretion model of Tuff et al. (2011). Note that, despite the fact that this model successfully reproduces the partitioning of Ni, Co, V, Cr and Nb between core and mantle, the calculated W and Mo partition coefficients are far from those required by the mantle concentrations of these elements. (Required value for W has been arbitrarily assigned an uncertainty of 25%).

der to derive expressions applicable over wider pressure ranges these authors also regressed $\log D_W$ against pressure, temperature, oxygen fugacity and $\left(\frac{NBO}{T}\right)$ simultaneously. This resulted in an apparent change of pressure dependence from positive (at 0.5–2 GPa) to negative with increasing pressure. We used a modified form of the approach of Cottrell et al. by taking account of our observation, discussed above, that the $\left(\frac{NBO}{T}\right)$ parameter is insufficient to represent adequately the silicate melt effects on partitioning of Mo. O'Neill et al. (2008) reached a similar conclusion for W dissolved in silicate melt, so we follow these authors in preferring the regular solution approach discussed above.

Our first step, as discussed above for Mo, was to perform a series of experiments at fixed pressure (1.5 GPa) and temperature (1923 K) in MgO capsules. Use of MgO leads to silicate melt composition which is almost constant. Oxygen fugacity was varied by changing the FeO content of the silicate melt. Taking this approach (Fig 5), and further restricting melt composition to a small range of NBO/T (2.5–2.7 NBO/T units) yields the following;

$$\log D_W + \log \gamma_W^{\text{met}} = -1.978(\pm 0.43) - 1.487(\pm 0.184) \log fO_2 \quad (18)$$

The best fit oxidation state, over the range 1.8–3.3 log units below IW is, therefore, at 1.5 GPa, +5.95 with a standard error of 0.7. i.e. +6 within uncertainty. For comparison, Cottrell et al. (2009) obtained oxidation states of between 4.7 and 5.5 for different subsets of their data between 0.5 and 2 GPa. Although W^{4+} must stabilise at very low oxygen fugacities, our data suggest no significant contribution by this oxidation state at any oxygen fugacity greater than IW-3 (Fig 5). For comparison, O'Neill et al. (2008) similarly found W^{4+} to be insignificant to about 3 log units below IW at 1400 °C/1 bar. The difference between our results and those of Cottrell et al. (2009) is, we consider, due firstly to the representation of silicate melt effects by the simplified parameter $\left(\frac{NBO}{T}\right)$ in the Cottrell et al.

study and secondly to the fact that all their experiments except one at pressure ≤ 2 GPa were performed in carbon capsules. Although Cottrell et al. (2009) applied corrections for Fe–W–C interactions using the same database as we employed (J.S.P.S., 1988) the effects are large and there are uncertainties associated with the extrapolation of Fe–W–C interactions to W concentrations well above the calibrated range of 0–24% W (Suzuki et al., 1970) and to very high temperature. We did not need to make these corrections because our system is C-free.

Cottrell et al. (2009) found that, with increasing pressure the apparent oxidation state of W declines from 4.7 (0.5–2 GPa) to 4.4 (6–18 GPa) and the pressure dependence of partitioning changes sign from positive to negative. They thus treated the pressure intervals separately in their fitting. In order to test whether this decline in oxidation state is robust, we added our 15 experimental data points at 6–24 GPa to the 6–18 GPa data set of Cottrell et al. (2009) and re-regressed the data using their equation. This yielded:

$$\begin{aligned} \log D_W = & 1.48(27) - 1.50(12) \log fO_2 - \frac{85(28)P}{T} \\ & - 0.80(09)(NBO/T) \\ \text{std error} = & 0.22; P > 6 \text{ GPa} \end{aligned} \quad (19)$$

Note that by adding data from our 15 experiments performed in MgO capsules the apparent valence of W changes from +4.4 (Cottrell et al., 2009) to +6.0. The other parameters in Eq. (19) are very similar to those reported by Cottrell et al. (2009). Specifically, we find an (NBO/T) term of $-0.80(09)$ compared to $-0.85(07)$, a constant of 1.48(27) compared to 2.10(48) and a pressure term of $-85(28)$ compared to $-112(13)$. We find the $(1/T)$ term to be statistically insignificant while Cottrell et al. derived $\frac{1128(1003)}{T}$, a term which is close to zero within uncertainty. Note also that the constant term, when the equation is converted to $RT \log K_D$ corresponds to an entropy term in the exchange reaction of +12.3(2.2) a value which is very close to the value obtained from end-member thermodynamic data (Barin et al., 1989) of 15 JK^{-1} . We conclude that this exercise successfully recovered the correct entropy term and pressure and compositional terms in excellent agreement with previous estimates which were based on smaller datasets. Furthermore we have demonstrated that we can assume a W oxidation state of +6 for the experimental oxygen fugacity range at pressures of 6–24 GPa and may formulate K_D accordingly.

Given that the oxidation state of W in the experimental pressure–temperature–oxygen fugacity range is, within uncertainty, +6, we can follow the same procedure as for Mo and formulate a W–Fe exchange coefficient as follows:

$$\begin{aligned} \log K_{\text{exch}} = & \log \frac{X_W^{\text{met}} \gamma_W^{\text{met}} (X_{\text{FeO}}^{\text{sil}} \gamma_{\text{FeO}}^{\text{sil}})^3}{X_{\text{WO}_3}^{\text{sil}} \gamma_{\text{WO}_3}^{\text{sil}} (X_{\text{Fe}}^{\text{met}} \gamma_{\text{Fe}}^{\text{met}})^3} \\ = & \log K_D + \log \frac{(\gamma_{\text{FeO}}^{\text{sil}})^3}{\gamma_{\text{WO}_3}^{\text{sil}}} \end{aligned} \quad (20)$$

Following Wade and Wood (2005) we fixed the temperature-dependence of the exchange coefficient from the end-member thermodynamic data of Barin et al. (1989) and

adopted a regular solution model for silicate melt effects (O'Neill and Eggins, 2002; O'Neill et al., 2008). We then regressed all of our data together with data from the literature (Hillgren et al., 1996; Jana and Walker, 1997; Ohtani et al., 1997; Cottrell et al., 2009; Righter et al., 2010) to determine the pressure dependence of partitioning in the range 0.5–24 GPa and the apparent regular solution parameters. Note that we excluded the 18 data from Cottrell et al. (2009) from experiments performed in W capsules at 2–2.3 GPa. This was because of uncertainties arising from using W–WO₂ in place of Fe–FeO to calculate oxygen fugacity. This leaves 156 data points at 0.5–24 GPa. The resultant fit, illustrated in Figs 6 and 7 is:

$$\begin{aligned} RT \log K_D^W = & -73730(6030) + 7.4(1.2) \times 10^4 X_{\text{SiO}_2}^2 - 6.3(1.2) \\ & \times 10^4 X_{\text{MgO}} + 1.1(0.3) \times 10^5 X_{\text{MgO}} X_{\text{SiO}_2} \\ & - 7.3(1.0) \times 10^5 X_{\text{CaO}}^2 + 1.73(0.49) \times 10^5 X_{\text{FeO}}^2 \\ & + 2.2(0.3) \times 10^6 X_{\text{AlO}_{1.5}} X_{\text{CaO}} + 15T - 640(80)P \\ & \text{std error} = 4.9 \text{ kJ} \end{aligned} \quad (21)$$

When converted to MORB–pyrolite composition, this expression becomes:

$$\log K_D^W = 1.80 - \frac{6728}{T} - \frac{77P}{T} \pm 0.24 \quad (22)$$

For peridotite the weight K_D for W, defined as follows, is about 12% larger than the mole K_D :

$$\begin{aligned} (D_W^{\text{wt}}) = \frac{[W]_{\text{met}}}{[W]_{\text{sil}}}; (D_{\text{Fe}}^{\text{wt}}) = \frac{[\text{Fe}]_{\text{met}}}{[\text{Fe}]_{\text{sil}}}; (K_D^{\text{wt}})_{\text{wt}} = \frac{(D_W^{\text{wt}})}{(D_{\text{Fe}}^{\text{wt}})^3} \\ \cong 1.12(K_D^{\text{wt}})_{\text{mol}} \end{aligned}$$

This translates, from Eq. (22) to the following expression for weight K_P :

$$\log (K_D^{\text{wt}})_{\text{wt}} = 1.85 - \frac{6728}{T} - \frac{77P}{T} \pm 0.24 \quad (23)$$

Note that the pressure term fitted to all data between 0.5 and 24 GPa is 77 with a standard error of 10. This compares to the fit from 6–24 GPa using the Cottrell et al. (2009) equation of 85 with a standard error of 28. Therefore the pressure term derived from fitting all the data is no different, within uncertainty, from that applicable to the data from 6–24 GPa and there is no clear evidence for a change in slope of the pressure dependence at about 6 GPa.

4. DISCUSSION

The core–mantle partition coefficient for Fe in the Earth, by weight, is estimated to be about 13.6 (McDonough and Sun, 1995; McDonough, 2003) while a new value of the W content of the silicate Earth of 12 ppb (König et al., 2011) leads to D_W (core/mantle) of approximately 40. Mo was more siderophile than W during core-formation with core–mantle partition coefficients in the range 90–140 (McDonough, 2003; Palme and O'Neill, 2003). These constraints, when coupled with our Mo and W partitioning relationships may be used to test models of Earth accretion and core segregation. We follow Wade and Wood (2005) in

treating the data in terms of continuous accretion and core segregation in the growing Earth.

4.1. Continuous Earth accretion models

The principal features of continuous accretion models (Wade and Wood, 2005; Wood et al., 2006; Tuff et al., 2011) are that the core was segregated continuously and that the pressure and temperature of metal segregation increased monotonically as the Earth grew. Wade and Wood (2005) argued that, since the maximum pressures of metal segregation derived from metal silicate partitioning data are only about 30–40% of the core–mantle boundary pressure, the lower mantle must have been largely solid during metal segregation with the temperature of metal–silicate equilibration close to that of the silicate liquidus. In a recent paper (Tuff et al., 2011) we determined the effects of Si dissolved in the metal on the metal–silicate partitioning of Mo, W, Ni, Co, V, Cr and Nb and modified the continuous accretion model to take account of these effects. Broadly speaking the addition of Si-metal interactions changes the best-fit model slightly, but the principal features described by Wade and Wood (2005) remain (see Fig 7, Tuff et al., 2011). That is, that assuming that each increment of metal added to the growing Earth completely equilibrated with the mantle, the concentrations of Ni, Co, W, Cr, V and Nb in the mantle can be explained by metal–silicate partitioning data provided the Earth became more oxidised as it grew. We used the continuous accretion model of Tuff et al. (2011) as the starting point for testing the implications of the new partitioning data presented here.

Fig. 8 shows the core–mantle partitioning behaviour of Mo and W calculated from Eqs. (16) and (23) for the model shown in Fig. 7 of Tuff et al. (2011). In this accretionary model the oxidised Fe content of the mantle increases in two steps from 1% to 3% and from 3% to 6.26% and the pressure of metal–silicate equilibration rises from 0 to 36 GPa as a fixed fraction of the depth to the core–mantle boundary in the growing planet. As can be seen, however, this model, which correctly reproduces the core–mantle partitioning of Ni, Co, Cr, V and Nb, predicts that W should be more strongly partitioned into the core than Mo i.e. the opposite of the observed relationship. The first reaction to this observation is that disequilibrium between accreting metal and silicate, as proposed by Rubie et al. (2003), must be responsible for the inversion of anticipated Mo/W ratios in the silicate Earth. The hypothesis of disequilibrium is, however, difficult to reconcile with the fact that W is calculated to be more siderophile than Mo throughout the accretion path depicted in Fig 8. We cannot, therefore, select any particular point on the path and assume that the metal and silicate at that point are mixed in disequilibrium into the core and mantle of the Earth thereby reproducing the Mo and W contents of the mantle. This will always lead to D_W/D_{Mo} which is too high and W contents of the mantle which are too low. After experimenting at length with the oxidation state of the Earth during accretion we concluded that resolution of this problem most plausibly resides in the concentrations of light elements in the core.

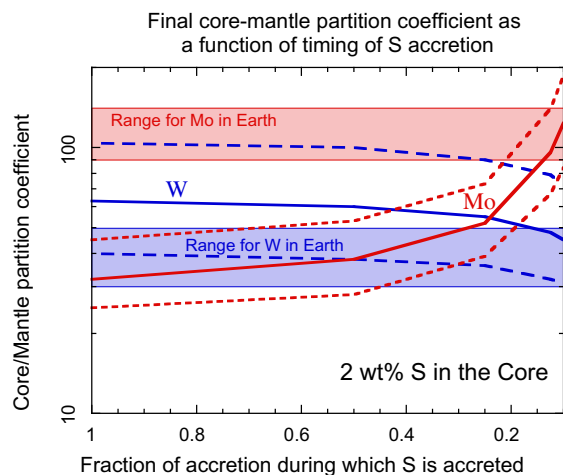


Fig. 9. Final core–mantle partition coefficients for Mo and W as a function of timing of S addition to the Earth. This calculation uses the same continuous accretion model as that used for Fig. 8 with the addition of 2% S to the core. As can be seen, addition of this S content in small amounts of S-rich metal towards the end of accretion has dramatic effects on the overall partitioning of Mo and W such that the required D values for Earth can be matched. Note that observed D_W (core/mantle) for Earth of 40 has been assigned an arbitrary uncertainty of ± 10 . See text for explanation of dramatic effect of sulphur.

Interaction parameters for the metal phase (Table 4) show that W interacts strongly with S in the metal while activities of Mo in this phase are little affected by its S content. Similarly, the strong negative interaction of S with itself ($\epsilon_S^S = -5.66$) means that the activity coefficient of Fe, the solvent, increases as the S content of the metal increases (Eq. (6)) while the positive interaction of S with Si ($\epsilon_{Si}^S = 9.16$) results in an increase of activity coefficient of Si as the S content increases. The net results are that increasing S content of the metal, at constant D_{Fe} , leads to decreasing D_W and D_{Si} and increasing D_{Mo} . The latter increase is partly caused by the fact that decreasing D_{Si} results in a lower Si content of the metal which, because Si–Mo interactions are strongly positive (Table 4) means Mo more strongly partitions into the metal. The S content of Earth’s core has been estimated as $\sim 1.7\%$ from cosmochemical abundances and by correlating siderophile S with lithophile Zn in silicate Earth (Dreibus and Palme, 1996). More recent experiments (Mann et al., 2009) indicate that Zn is actually slightly siderophile rather than completely lithophile under conditions of core formation which means that Dreibus and Palme (1996) estimate of the S content of the core may be slightly low. We have therefore rounded it up to 2% for the following discussion.

Fig. 9 shows the effects of changing the timing of S addition to the Earth on the overall core–mantle partitioning of Mo and W. This figure was constructed using the accretionary path depicted in Tuff et al. (2011), the sole change being that volatile S was added to the metal at different stages of the process. Thus, we find that if Earth’s sulphur were added at the same S/Fe ratio throughout accretion, the effects on Mo and W partitioning would have been negligible.

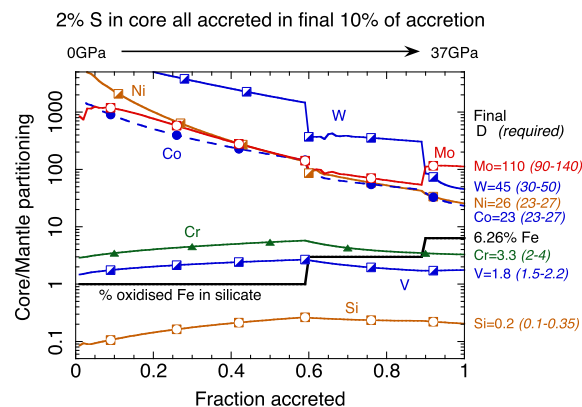


Fig. 10. An example of a continuous accretion model which matches the observed partitioning of a number of refractory elements between core and mantle of Earth. The oxidation path, in terms of %oxidised Fe in the silicate is exactly the same as for the example shown in Tuff et al. (2011). The only significant difference is the addition of 2% S to the core during the last 10% of accretion.

If, however, the early phases of accretion corresponded to S/Fe of zero with the later stages at high S/Fe then the relationships between D_W and D_{Mo} would have changed significantly. Fig. 9 shows that the required values of D_{Mo} and D_W would have been achieved if S was added to the Earth only during the last 10–20% of accretion. We therefore find, in agreement with conclusions reached from the Ag isotopic composition of silicate Earth (Schönbächler et al., 2010) that the Mo and W contents of the mantle constrain the timing of addition of moderately volatile elements such as S and Ag to the Earth. Specifically, S must have been added during the later stages of accretion, but while the core was still being segregated rather than as part of a “late veneer” (Wood et al., 2010). The principal remaining issue is how this late addition of S will affect the core–mantle partitioning of the other refractory elements discussed by Wade and Wood (2005) and Tuff et al. (2011).

Fig. 10 shows an accretionary path, modified slightly from Tuff et al. (2011), which correctly reproduces the observed concentrations of Mo, W, Ni, Co, V, and Cr in the silicate Earth. (Note that Nb was omitted from the figure for clarity but that the calculated overall D_{Nb} of 0.6 is also consistent with the expected value of Tuff et al. (2011). For simplicity we assumed changes in oxidised Fe content of the mantle at the same points as previously and added S only in the last 10% of accretion. In order to match the observed partitioning we needed to increase the maximum pressure of equilibration from 36 to 37 GPa. All partition coefficient relationships, apart from those for Mo and W, which are presented above, were taken from Table 6 of Tuff et al. (2011). The main feature to note is that the increase of Fe content of silicate Earth and of S content of the core at $\sim 90\%$ of accretion dramatically increases D_{Mo} and reduces D_W . The principal reasons are the effects of S on reducing the Si content of the metal being removed and on increasing the activity coefficients of W and Fe in the metal. Thus, this illustrative example shows how late accretion of sulphur leads to $D_{Mo} > D_W$ and appropriate

concentrations of Mo and W in silicate Earth. Late accretion of S has little effect on the overall partitioning of the other refractory elements Ni, Co, V, Cr and Nb.

5. CONCLUSIONS

At 1.5 GPa/1923 K we find that the oxidation state of Mo in MgO-rich silicate melt in equilibrium with Fe rich metal at oxygen fugacities between 1.9 and 3.1 log units below the Fe–FeO (IW) buffer is indistinguishable from +4. This result is in agreement with the data of Holzheid et al. (1994) who performed similar experiments at 1 bar/1673 K. In contrast to the results for Mo, we find that, at 1.5 GPa/1923 K, W has an oxidation state indistinguishable from +6 in similar MgO-rich melts at equivalent oxygen fugacities. This result is in general agreement with those of O'Neill et al. (2008) and Cottrell et al. (2009). Unlike the latter authors, however, we find evidence neither for a change in oxidation state of W as pressure is increased from 2 GPa to the 6–24 GPa range nor for a significant change in the pressure dependence of W partitioning. Our results are based on adding our 15 data points from experiments performed in the 6–24 GPa pressure range to those of Cottrell et al. (28 data at 6–18 GPa) and re-regressing using the same equation as that used by Cottrell et al. We recognise, of course, that under very highly reducing conditions W must adopt the +4 oxidation state. There is, however, no evidence for this in the oxygen fugacity range above IW-3 (3 log units below IW) at pressures to 24 GPa.

The metal–silicate partitioning of both Mo and W is sensitive to the compositions of metal and silicate phases. In order to correct for the effects of elements other than Fe in the liquid metal phase we used the epsilon model with interaction parameters taken from the literature (J.S.P.S., 1988). For Mo in silicate melts we find that the simplified non-bridging oxygen/tetrahedral cation ($\frac{NBO}{T}$) model is inadequate to represent the variation of activity with composition. We therefore followed O'Neill and Eggins (2002) in adopting a regular solution model for both Mo and W dissolved in silicate melt.

We combined our results, obtained at pressures of 1.5–24 GPa and temperatures of 1803–2723 K, with data from the literature to parameterize the partition coefficients of Mo and W as functions of silicate composition, pressure, temperature and the partition coefficient of Fe (equivalent to oxygen fugacity). The partition coefficient relationships were then used in conjunction with the continuous Earth accretion model of Wade and Wood (2005) to calculate expected core–mantle partitioning of Mo and W at the end of accretion. Surprisingly, if we allow pressure, temperature and oxygen fugacity to increase during accretion in ways consistent with the core–mantle partitioning of a number of other refractory siderophile elements (Tuff et al., 2011) we find that W should be more siderophile than Mo (Fig 8). This is the reverse of the relationship actually observed for the Earth. Furthermore, allowing a certain amount of metal–silicate disequilibrium during core segregation does not readily bring the core–mantle partitioning relationships into agreement with those observed.

After considering the effects of the light element in the core on metal–silicate partitioning we find that the simplest model which maintains the observed core–mantle partitioning of Ni, Co, V, Cr, Nb and brings the Mo and W partitioning into agreement with that observed is one in which S is added to the Earth towards the end of accretion rather than at a constant rate throughout accretion. Specifically, adding a total of about 2% S to the metal has a large effect at the end of accretion if, for example the last 10% of metal added to the core contains ~20% S. Interaction parameters for the metal phase (Table 4) show that W interacts strongly with S in the metal while activities of Mo in this phase are little affected by its S content. Similarly, the strong negative interaction of S with itself ($\epsilon_S^S = -5.66$) means that the activity coefficient of Fe, the solvent, increases as the S content of the metal increases (Eq. (6)) while the positive interaction of S with Si ($\epsilon_{Si}^S = 9.16$) results in an increase of activity coefficient of Si as the S content increases. The net results are that increasing S content of the metal, at constant D_{Fe} , leads to decreasing D_W and D_{Si} and increasing D_{Mo} . The latter increase is partly caused by the fact that decreasing D_{Si} results in a lower Si content of the metal which, because Si–Mo interactions are strongly positive means Mo more strongly partitions into the metal.

We conclude that, given an S content of the core of ~2% (Dreibus and Palme, 1996), S and other elements of similar volatility such as Pb and Zn were accreted to the Earth near the end of planetary growth rather than at a constant rate throughout accretion.

ACKNOWLEDGEMENTS

We acknowledge the support of the NERC (UK) through award NE/F018266/1 and the STFC (UK) through rolling Grant ST/G00272X/1. The manuscript was greatly improved by the reviews of Mike Walter, Wim van Westrenen and an anonymous reviewer.

REFERENCES

- Allège C. J., Poirier J.-P., Humler E. and Hofmann A. W. (1995) The chemical composition of the Earth. *Earth Planet. Sci. Lett.* **134**, 515–526.
- Barin I., Sauert F., Schultze-Rhonhof E. and Sheng W. S. (1989) *Thermochemical data of pure substances, Part I and Part II*. CH Verlagsgesellschaft, Weinheim, Germany.
- Bohlen S. R. and Boettcher A. L. (1982) The quartz coesite transformation: a precise determination and the effects of other components. *J. Geophys. Res.* **87**, 7073–7078.
- Chabot N. L. and Drake M. J. (1999) Potassium solubility in metal: the effects of composition at 15 kbar and 1900 °C on partitioning between iron alloys and silicate melts. *Earth Planet. Sci. Lett.* **172**, 323–335.
- Corgne A., Keshav S., Wood B. J., McDonough W. F. and Fei Y. (2008) Metal–silicate partitioning and constraints on core composition and oxygen fugacity during Earth accretion. *Geochim. Cosmochim. Acta* **72**, 574–589.
- Cottrell E., Walter M. J. and Walker D. (2009) Metal–silicate partitioning of tungsten at high pressure and temperature: implications for equilibrium core formation in Earth. *Earth Planet. Sci. Lett.* **281**, 275–287.

- Dreibus G. and Palme H. (1996) Cosmochemical constraints on the sulfur content in the Earth's core. *Geochim. Cosmochim. Acta* **60**, 1125–1130.
- Falloon T. J. and Green D. H. (1987) Anhydrous partial melting of MORB pyroxene and other peridotite compositions at 10 kb: implications for the origin or primitive MORB glasses. *Contrib. Mineral. Petrol.* **37**, 181–219.
- Helffrich G. and Wood B. J. (1989) Subregular model for multicomponent solutions. *Am. Mineral.* **74**, 1016–1022.
- Hillgren V. J., Drake M. J. and Rubie D. C. (1996) High pressure and high temperature metal–silicate partitioning of siderophile elements: the importance of silicate liquid composition. *Geochim. Cosmochim. Acta* **60**, 2257–2263.
- Holland T. J. B. (1980) The reaction albite = jadeite + quartz determined experimentally in the range 600–1200 °C. *Am. Mineral.* **65**, 129–134.
- Holzheid A., Borisov A. and Palme H. (1994) The effect of oxygen fugacity and temperature on solubilities of nickel, cobalt, and molybdenum in silicate melts. *Geochim. Cosmochim. Acta* **58**, 1975–1981.
- Jana D. and Walker D. (1997) The influence of silicate melt composition on the distribution of siderophile elements among metal and silicate liquids. *Earth Planet. Sci. Lett.* **150**, 463–472.
- Kegler P., Holzheid A., Frost D. J., Rubie D. C., Dohmen R. and Palme H. (2008) New Ni and Co metal–silicate partitioning data and their relevance for an early terrestrial magma ocean. *Earth Planet. Sci. Lett.* **268**, 28–40.
- König S., Münker C., Hohl S., Paulick H., Barth A. R., Lagos M., Pfänder J. and Büchl A. (2011) The Earth's tungsten budget during mantle melting and crust formation. *Geochim. Cosmochim. Acta* **75**, 2119–2136.
- Li J. and Agee C. B. (1996) Geochemistry of mantle–core differentiation at high pressure. *Nature* **381**, 686–689.
- Ma Z. T. (2001) Thermodynamic description for concentrated metallic solutions using interaction parameters. *Metall. Mater. Trans. B* **32**, 87–103.
- Mann U., Frost D. J. and Rubie D. C. (2009) Evidence for high-pressure core–mantle differentiation from the metal–silicate partitioning of lithophile and weakly-siderophile elements. *Geochim. Cosmochim. Acta* **73**, 7360–7386.
- McDade P., Wood B. J., Westrenen W. V., Brooker R., Gudmundsson G., Soular H., Najorka J. and Blundy J. (2002) Pressure corrections for a selection of piston–cylinder cell assemblies. *Mineral. Mag.* **66**, 1021–1028.
- McDonough W. F. (2003) Compositional model for the Earth's core. In *The Mantle and Core* (ed. R. W. Carlson). Elsevier–Pergamon, Oxford.
- McDonough W. F. and Sun S.-s. (1995) The composition of the Earth. *Chem. Geol.* **120**, 223–253.
- Mills K. C. (1993) Influence of structure on the physico-chemical properties of slags. *ISIJ Int.* **33**, 148–155.
- O'Neill H. S. C., Berry A. J. and Eggins S. M. (2008) The solubility and oxidation state of tungsten in silicate melts: implications for the comparative chemistry of W and Mo in planetary differentiation processes. *Chem. Geol.* **255**, 346–359.
- O'Neill H. S. C. and Eggins S. M. (2002) The effect of melt composition on trace element partitioning: an experimental investigation of the activity coefficients of FeO, NiO, CoO, MoO₂ and MoO₃ in silicate melts. *Chem. Geol.* **186**, 151–181.
- Ohtani E., Yurimoto H. and Seto S. (1997) Element partitioning between metallic liquid, silicate liquid, and lower-mantle minerals: implications for core formation of the Earth. *Phys. Earth Planet. In.* **100**, 97–114.
- Palme H. and O'Neill H. S. C. (2003) Cosmochemical estimates of mantle composition. In *The Mantle and Core* (ed. R. W. Carlson). Elsevier, Amsterdam.
- Presnall D. C., Dixon S. A., Dixon J. R., O'Donnell T. H., Brenner N. L., Schrock R. L. and Dycus D. W. (1978) Liquidus phase relations on the join diopside–forsterite–anorthite from 1 atm to 20 kbar: their bearing on the generation and crystallization of basaltic magma. *Contrib. Mineral. Petrol.* **66**, 203–220.
- Righter K. (2003) Metal–silicate partitioning of siderophile elements and core formation in the early Earth. *Annu. Rev. Earth Planet. Sci.* **31**, 135–174.
- Righter K. and Drake M. J. (1997) Metal–silicate equilibrium in a homogeneously accreting earth: new results for Re. *Earth Planet. Sci. Lett.* **146**, 541–553.
- Righter K., Pando K. M., Danielson L. and Lee C.-T. (2010) Partitioning of Mo, P and other siderophile elements (Cu, Ga, Sn, Ni, Co., Cr, Mn, V and W) between metal and silicate melt as a function of temperature and silicate melt composition. *Earth Planet. Sci. Lett.* **291**, 1–9.
- Rubie D. C., Melosh H. J., Reid J. E., Liebske C. and Righter K. (2003) Mechanisms of metal–silicate equilibration in the terrestrial magma ocean. *Earth Planet. Sci. Lett.* **205**, 239–255.
- Rudge J. F., Kleine T. and Bourdon B. (2010) Broad bounds on Earth's accretion and core formation constrained by geochemical models. *Nat. Geosci.* **3**, 439–443.
- Schönbächler M., Carlson R. W., Horan M. F., Mock T. D. and Hauri E. H. (2010) Heterogeneous accretion and the moderately volatile element budget of Earth. *Science* **328**, 884–887.
- J.S.P.S. (1988) *Steelmaking Data Sourcebook*. Gordon and Breach, New York.
- Suzuki Y., Ban-Ya S. and Fuwa T. (1970) Activity of carbon and oxygen in liquid iron alloys. *Tetsu-To-Hagane* **56**, 1809–1818.
- Thibault Y. and Walter M. J. (1995) The influence of pressure and temperature on the metal–silicate partition coefficients of nickel and cobalt in a model C1 chondrite and implications for metal segregation in a deep magma ocean. *Geochim. Cosmochim. Acta* **59**, 991–1002.
- Tuff J., Wood B. J. and Wade J. (2011) The effect of Si on metal–silicate partitioning of siderophile elements and implications for the conditions of core formation. *Geochim. Cosmochim. Acta* **75**, 673–690.
- Wade J. and Wood B. J. (2005) Core formation and the oxidation state of the Earth. *Earth Planet. Sci. Lett.* **236**, 78–95.
- Wagner C. (1962) *Thermodynamics of Alloys*. Addison-Wesley, Reading, Ma.
- Walker D. (1991) Lubrication, gasketing and precision in multianvil experiments. *Am. Mineral.* **76**, 1092–1100.
- Walker D., Carpenter M. A. and Hitch C. M. (1990) Some simplifications to multianvil devices for high pressure experiments. *Am. Mineral.* **76**, 1020–1028.
- Walter M. J. and Thibault Y. (1995) Partitioning Of Tungsten And Molybdenum Between Metallic Liquid And Silicate Melt. *Science* **270**, 1186–1189.
- Wood B. J., Halliday A. N. and Rehkämper M. (2010) Volatile accretion history of the Earth. *Nature* **467**. doi:10.1038/nature09484.
- Wood B. J., Walter M. J. and Wade J. (2006) Accretion of the Earth and segregation of its core. *Nature* **441**, 825–833.
- Yagi T., Akaogi M., Shimimura O., Suzuki T. and Akimoto S. (1987) In situ observation of the olivine–spinel phase transformation in Fe₂SiO₄ using synchrotron radiation. *J. Geophys. Res.* **92**, 6207–6213.